Large-Eddy Simulation of a Supersonic Air Inlet in Subcritical Regime

Pierre Grenson, Samir Beneddine

Association Aéronautique et Astronautique de France

55th 3AF International Conference on Applied Aerodynamics
23 — 25 March 2020, Poitiers – France

FP51-2020-GRENSON

Large-Eddy Simulation of a Supersonic Air Inlet in Subcritical Regime

Pierre Grenson[(1)] and Samir Beneddine[(2)]

[(1)]*Onera, The French Aerospace Lab, 8, rue des Vertugadins 92190, pierre.grenson@onera.fr*

[(2)]*Onera, The French Aerospace Lab, 8, rue des Vertugadins 92190, samir.beneddine@onera.fr*

ABSTRACT

The present paper reports on the wall-resolved Large-Eddy Simulation (LES) of a rectangular supersonic air inlet at Mach number 1.8. The peculiarity of the investigated configuration is the presence of a flat plate on which develops a turbulent boundary layer upstream of the first compression ramp. Two modes exhibiting low-frequency flow unsteadiness in the subcritical regime have been simulated: the little buzz (low amplitude oscillations) and the big buzz (large amplitude oscillations). A detailed analysis is performed on the spectral content of the flow and the pressure fluctuations in the duct in order to understand the underlying flow mechanisms. It is shown that the physical phenomena are similar in both cases with appearance of downstream-propagating expansion waves and upstream-propagating compression wave that are related to the terminal shock back-and-forth motion.

1. INTRODUCTION

The role of a supersonic air inlet is to decelerate the incoming supersonic air to a low subsonic flow required for proper work of the engine (turbojet or ramjet). This operation must induce the minimum possible total pressure losses while ensuring a stable flow regime. As first observed by Oswatitsch in 1944, the shock system ahead of the air intake may suffer from large oscillations when the mass flow rate required by the engine is reduced below a certain threshold. This phenomenon, referred to as buzz, is highly undesirable as it can strongly alter the engine thrust or lead to unacceptable structural loads.

From experimental observations on axisymetric air inlets, Ferri[7] et Dailey[5] have related its occurence to either the ingestion of the shear layer due to shock intersection ahead of the inlet section or to the flow separation on the compression due to the shock boundary layer interaction (SWBLI). From then on, many experimental studies [14, 2] have highlighted the occurrence of buzz phenomena for different inlet shape (axisymmetric, rectangular). Depending on the inlet geometry and freestream condition, they have shown that the violent buzz with large oscillations, generally called *big buzz*, can be preceded in the throttling process by small oscillations of the shock system, called *little buzz*.

Since the advent of the computational fluid dynamics, several numerical studies have focused on buzz phenomena. Different works [11, 9, 3] have shown that unsteady RANS (Reynolds-Averaged Navier-Stokes) can predict the flow oscillations related to the big buzz, with fair estimation of its frequency. They have been few reported attempts to apply high-fidely approaches which directly solve a part of the turbulent spectrum. Trapier *et al.*[13] have simulated the big buzz of a rectangular air inlet by means of the hybrid RANS-LES method DDES. Candon *et al.*[1] have investigated the flow oscillations near the critical regime of a axisymmetric air inlet thanks to an hybrid RANS-LES method. In a recent study[8], we have shown that the use of ZDES on a rectangular air inlet allowed to reproduce shock oscillations related to the little buzz, which was not possible with URANS simulations. In the aforementioned studies, the attached turbulent boundary layer is modelled by a RANS model. To the author's knowledge, there is no reported wall-resolved Large-Eddy Simulation (LES) of a supersonic air inlet, certainly due to the high Reynolds number encountered in industrial applications and the low frequency character of the buzz phenomena which requires long simulation time to converge spectral content. The purpose of the present work consists in using LES to investigate both the big and little buzz occurring for a small-scale rectangular supersonic air inlet in subcritical regime. The selected configuration is derived from a geometry which have been shown experimentally to exhibit little buzz prior to big buzz during the

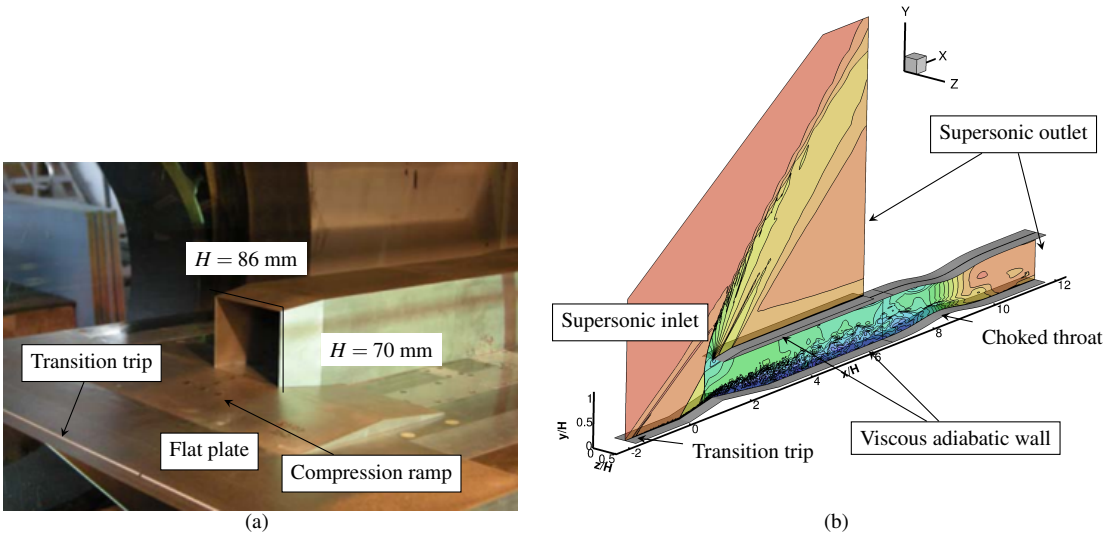

Figure 1: Investigated supersonic air inlet. (a) Photograph of the experimental configuration. (b) Computational setup.

throttling process. In this paper we first present the computational setup that has been selected (Sec. 2) and then perform an in-depth analysis of the flow behaviour for the two simulated regimes (Sec. 3.2) after having verified the proper resolution of the upstream turbulent boundary layer (Sec. 3.1).

2. COMPUTATIONAL SETUP

The experimental configuration is described in Fig. 1a. The rectangular air inlet of captation height H is preceded by a 10°-compression ramp and a flat plate of length $1.785H$. The transition of the boundary layer that develops from the flat plate leading edge is triggered by means of a roughness band (CADCUT) in order to ensure a fully turbulent state ahead of the compression ramp. The inlet inner cowl is aligned with freestream direction. The inlet diffuser has a rectangular cross section over a length $3H$. The diffuser ramp downstream of the inlet has a angle of 4°. It then evolves progressively towards a circular cross-section at the end of the duct where a conical plug allows to control the ingested mass flow ratio.

The simulated air inlet, illustrated in Fig. 1b, and flow conditions, gathered in Tab. 1, have been altered from the experimental configuration in order to make it tractable for LES with the available computing resources. First, the side walls have been removed and the flow is considered as homogeneous in transverse direction (Oz). Second, the overall geometry has been scaled down by a factor 7 in order to reduce the gap between the low frequency of the buzz phenomena, which has been shown in past studies to scale well with geometric dimensions, and the high frequency of turbulence. In order to guarantee that the boundary layer is still turbulent on the flat plate, the stagnation pressure has been raised by 75%.

Quantity	Experiments	CFD
H	70 mm	10 mm
$p_{i,\infty}$	175 kPa	300 kPa
p_∞	30 kPa	52 Pa
$T_{i,\infty}$	310 K	310 K
δ/H at $x=0$	4.1%	5.1%
Inlet width	$1.22H$	$0.5H$
Re_{δ_2} at $x=0$	2500	830

Table 1: Comparison of experimental and CFD parameters.

The equivalent incompressible Reynolds number

$$\mathrm{Re}_{\delta_2} = \mu_\infty/\mu_w \mathrm{Re}_\theta$$

of the simulated configuration is then reduced by almost a factor 3 with respect to the experimental geometry. Despite these differences, we have verified that the relative boundary layer thickness δ/H ahead of the compression ramp is similar in both cases.

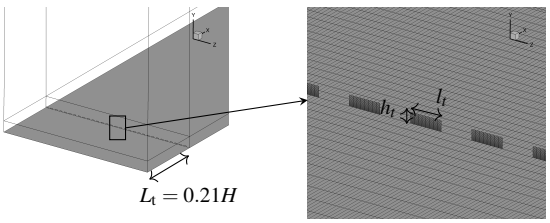

Figure 2: Numerical rough patch to trigger turbulence on the upstream flat plate.

The ingested mass flow ratio is controlled in the simulation by means of a chocked throat located at the same

relative longitudinal location as the plug in the experiments ($x = 8.5H$). The throat cross section area is expressed by the Throttling Ratio (TR) TR $= h_{ct}/H$, with h_{ct} the height of the throat. The size of the computational domain and the boundary conditions are shown in Fig. 1b with a snapshot of the instantaneous Mach number field obtained for $TR = 0.72$. At the supersonic inlet boundary condition, a uniform profile of the five conservative variables is prescribed.

In the same way as in the experiments, the transition of the laminar boundary layer that grows from the flat plate leading edge is triggered by means of a numerical rough patch (see Fig. 2) located at the same streamwise location L_t as that of the CADCUT. The patch is formed by zero-thickness crenel-like vertical wall of height h_t that does not excess 1.2 times the displacement thickness δ_1 of the laminar boundary layer in order to minimize their influence on the turbulent boundary layer properties. The gap length l_t between two adjacent vertical walls has been determined by trial-and-error so that the transition of the boundary layer is efficiently triggered. The height of the roughness element is discretized by 21 cells and its span by 8 cells.

The computational mesh is obtained by extrusion over 600 planes along z-axis of the 2D mesh in Oxy plane which is presented in Fig. 3. The grid refinement is con-

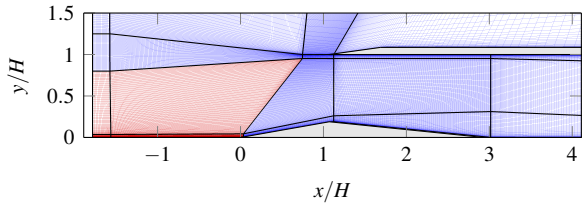

Figure 3: Discretization grid and structured blocks in Oxy plane. Only one point over two is represented.

centrated near the walls (flat plate, compression ramp, diffuser upper and lower wall) in order to properly resolve the most energetic turbulent scales. The cell size in wall units are at most $\Delta x^+ = 30$, $\Delta y^+ = 2$ and $\Delta z^+ = 10$, which is slightly better than classical LES resolution. Cells are also clustered along the shear layer associated with the expected flow separation due to the SWBLI and diffuser ramp flow deviation. As the position of this shear layer is likely to evolve depending on either the throttling ratio or the time during a buzz cycle, clustering is performed over a certain extent in height. The chosen discretization allows to fulfill the classical criteria for mixing layer based on the vorticity thickness $\delta_\omega = \frac{(u_{x,\max} - u_{x,\min})}{\partial u_x / \partial y_{\max}}$. Δ_x varies from $0.005\delta_\omega$ at the inlet section to $0.5\delta_\omega$ at the end of the diffuser, Δ_y is approximately $1/15\delta_\omega$ over the diffuser and $\Delta_z \sim 0.01\delta_\omega$. The final mesh is constituted of 350 millions cells, including 100 millions in the blocks associated to the upstream boundary layer.

The compressible Navier-Stokes equations are solved by means of the structured multi-block solver FastS, developed at Onera. No explicit subgrid-scale modelling is used as the dissipation of the unresolved turbulent structures is achieved by the numerical dissipation of the scheme. The spatial discretization is realized by the AUSM+(P) numerical scheme [10] which is second-order accurate. A sensor that deactivates the numerical dissipation term when spurious oscillations are detected is applied in the blocks ahead of the compression ramp (red blocks in Fig. 3) in order to not attenuate the flow perturbations generated by the roughness patch. Time-integration is carried out by means of the second-order-accurate backward scheme of Gear whose associated nonlinear system is iteratively solved at every time step by a Newton process with 5 inner iterations, resulting in a reduction of the residuals of approximately two orders of magnitude. The selected strategy has been proven successfull for the transonic buffet prediction [6], which has similar features to that investigated in this study (shock boundary layer interaction, large amplitude flow unsteadiness). The selected time step is $\Delta t = 1 \times 10^{-8}$ s, which corresponds to a maximal value of the CFL number of 5 in the boundary layers and a non-dimensional time step $\Delta t^+ = u_\tau^2 \Delta t / \nu_w$ of 0.2, well below the criterion $\Delta_t^+ < 1$ of Choi and Moin [4] for wall-bounded flows.

Computations have been performed on the Bull cluster Occigen (GENCI). Calculation domain has been split in 1700 blocks, balanced onto 1500 Intel Xeon Broadwell E5-2690v4 cores. Effective CPU cost per iteration per cell was $0.3\,\mu$s which led to a cost of roughly 20000 CPU hours per buzz cycle (about 200 000 time iterations).

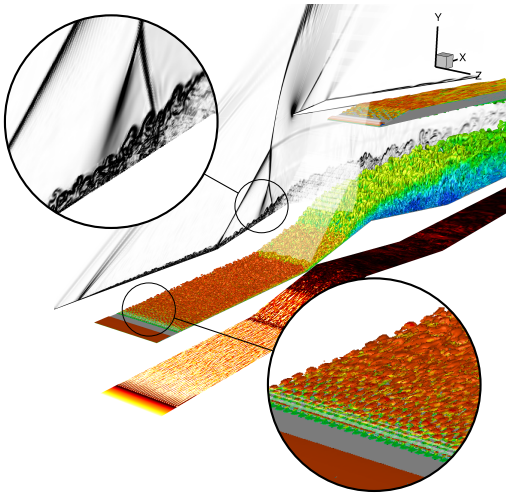

Figure 4: 3D view of the instantaneous flow field. Q-criterion colored by the axial velocity. (Left plane) Numerical Schlieren on a longitudinal slice cut. (Bottom surface) Wall skin friction coefficient.

3. RESULTS

This section is devoted to the analysis of the two simulations that have been conducted for little and big buzz respectively. Prior to this analysis, we validate the proper resolution of the incoming boundary layer ahead of the compression ramp.

3.1 Incoming turbulent boundary layer

Fig. 4 shows a three dimensional view of the instantaneous flow field of the LES simulation for TR = 0.72. The Q-criterion allows to demonstrate the efficiency of the numerical rough patch to trigger a rapid transition to turbulence on the flat plate. Fig. 5 presents the time-averaged velocity field above the flat plate along with boundary layer thicknesses which show its progressive streamwise growth. The presence of the transition trip in the uniform supersonic flow produces a little decrease (-0.5%) in the external Mach number, as illustrated by the white line in Fig. 5.

In Figs. 6 and 7, we compare the wall-resolved turbulent boundary layer to reference data from the litterature and in particular the Direct Numerical Simulation (DNS) of Schlatter *et al.* [12] of an incompressible boundary layer. It is seen in Fig. 6 that both the incompressible skin friction coefficient and shape factor of the present LES tend toward the reference data after a readaptation length, characterized by the distance from the transition trip relative to the boundary layer thickness at the transition location δ_0. Fig. 7 shows that the mean and fluctuating velocity profiles at a section ahead of the compression ramp are in a excellent agreement with the reference DNS.

Fig. 8 presents the power spectral density (PSD) of the longitudinal velocity component for two probes within the BL: one close to the transition trip (probe A) and the other one ahead of the compression ramp (probe B). Probe A exhibits two peaks in the PSD that can be associated with the shedding frequency in the wake of the roughness patch. For probe B, the peaks have disappeared and the PSD exhibits the classical inertial range prior to the cuff-off frequency of ≈ 3 MHz due to the numerical scheme and the mesh resolution.

3.2 Comparison of the two regimes

It is not possible to determine a priori the exact throttling ratios which allow to reproduce both regime and the flow regime has been proven very sensitive to this parameter. We have then performed a trial-and-error process to find the TR. Finally, little buzz regime has been reproduced for TR = 0.72 and the big buzz regime for TR = 0.70. The flow regime is first determined by inspecting the time evolution of the mass flow ratio through at the end of the subsonic diffuser (this location is called AIP in the following for Aerodynamic Interface Plane), represented in Fig. 9a. The big buzz regime is characterized by large amplitude variations of the normalized mass flow rate whereas the little buzz regime features low amplitude fluctuations. Contrary to the little buzz, the periodic behavior of big buzz is quite visible. The simulated physical time of little and big buzz spans respectively 13 and 6 characteristic times, the latter being defined as the period corresponding to a frequency of 500 Hz.

The power spectral density (PSD) of the mass flow rate for both regimes is plotted in Fig. 9b. The big buzz regime presents a clear frequency peak at 450 Hz whereas little buzz exhibits a milder peak at a slightly higher frequency of ≈ 580 Hz. Both frequencies are of the same order as that was observed in the experiments multiplied by 7 (the scale factor between the real configuration and the simulated one), namely $83\,\text{Hz} \times 7 = 581\,\text{Hz}$ for big buzz and $107\,\text{Hz} \times 7 = 749\,\text{Hz}$ for little buzz.

Fig. 10 compares the time-averaged distribution of the pressure coefficient on the lower wall. For both regimes, it seen that the mean pressure is first strongly increased because of both the ramp (R) shock and the terminal shock and then further raised in the subsonic diffuser from the inlet section (I) until the AIP. The pressure then decreases because of the flow acceleration in the chocked convergent-divergent throat (T). As shown in Fig. 10 where the RMS envelope have also been plotted, little and big buzz regimes do not experience the same level of fluctuations in the duct, with greater amplitude for the big buzz. Besides, one could notice that there is almost no pressure fluctuation at the throat for both cases. This is coherent with the hypothesis generally assumed that the throat acts as a fixed pressure impedance boundary condition.

Following the proposal of Newsome [11], we have tried to correlate the observed frequencies with that corresponding to the fundamental frequency of an open-closed duct of constant cross section area and length L given by:

$$f_0 = \frac{c}{4L}\left(1 - M^2\right) \tag{1}$$

with M being the mean Mach number in the duct. The length L is taken as the distance between the inlet section and the choked throat, namely $7.43H$. According to Tab. 2, it turns out that the observed frequencies are significantly lower than the estimated fundamental frequency of the duct. In the litterature [14], observed and estimated frequencies generally match better. In the following, we will perform an in-depth analysis of the flow dynamics for both regimes in order to explain these discrepancies.

3.2.1 Little buzz

The mean and fluctuating velocity fields are represented in Fig. 11 along with a numerical Schlieren visualization

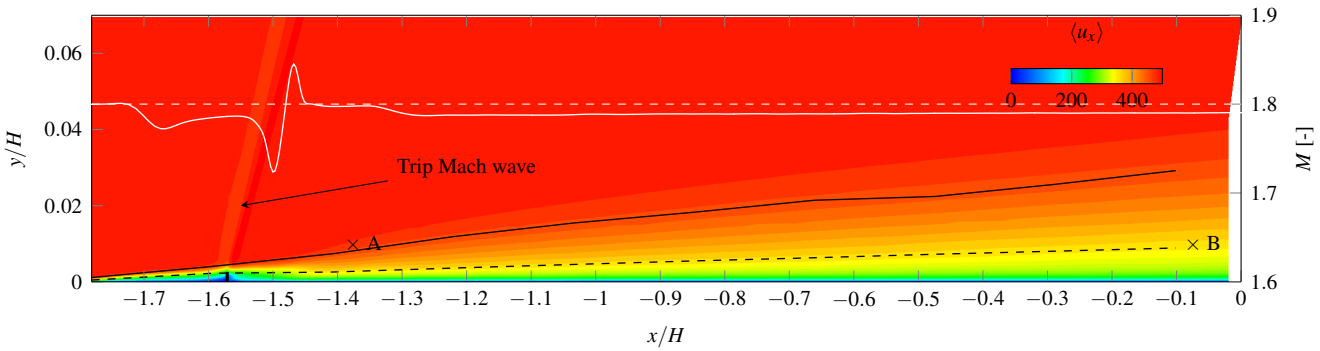

Figure 5: Close-up view on the upstream flat plate (vertical axis has been enlarged). Time-averaged longitudinal velocity field. (——) Boundary layer thickness $\delta_{0.95}$. (- - -) Boundary layer displacement thickness δ_1. The vertical marker illustrates the trip location and real geometry. (Solid white line) Evolution of the Mach number at $y/H = 0.065$.

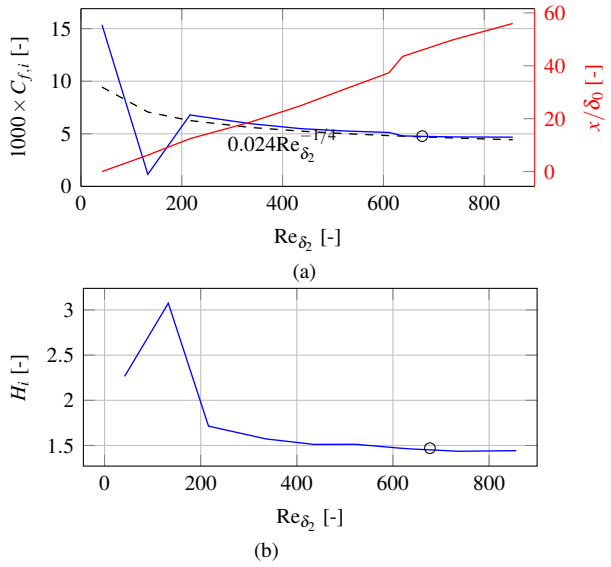

Figure 6: Characteristic boundary layer properties evolution. (- - -) Smits' law. (——) Present LES. (○) DNS.

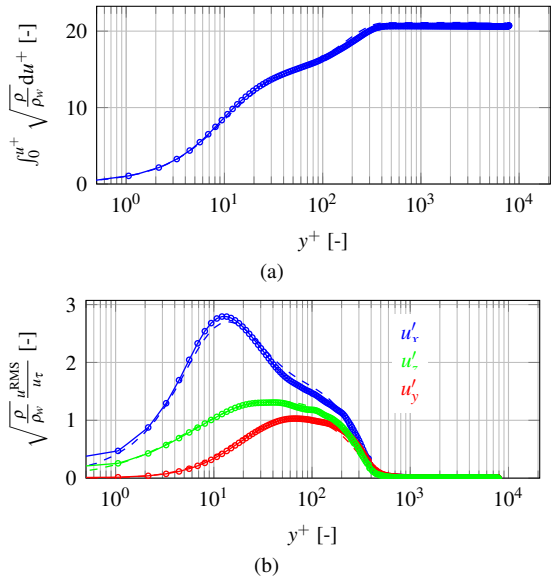

Figure 7: Time-averaged (a) and root-mean-squared (b) velocity at different longitudinal location. (—○—) Present LES. (- - -) DNS.

Regime	M	LES	f_0
Little buzz (TR = 0.72)	0.56	623 Hz	776 Hz
Big Buzz (TR = 0.70)	0.55	450 Hz	788 Hz

Table 2: Estimated and observed main oscillation frequency for both regimes.

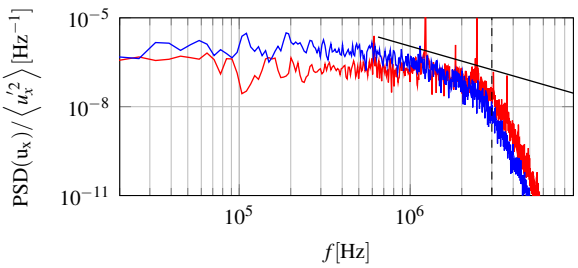

Figure 8: Longitudinal velocity PSD for two probes in the boundary layer.(——) Probe A. (——) Probe B. See Fig. 5 for probe location. (——) -5/3 power law.

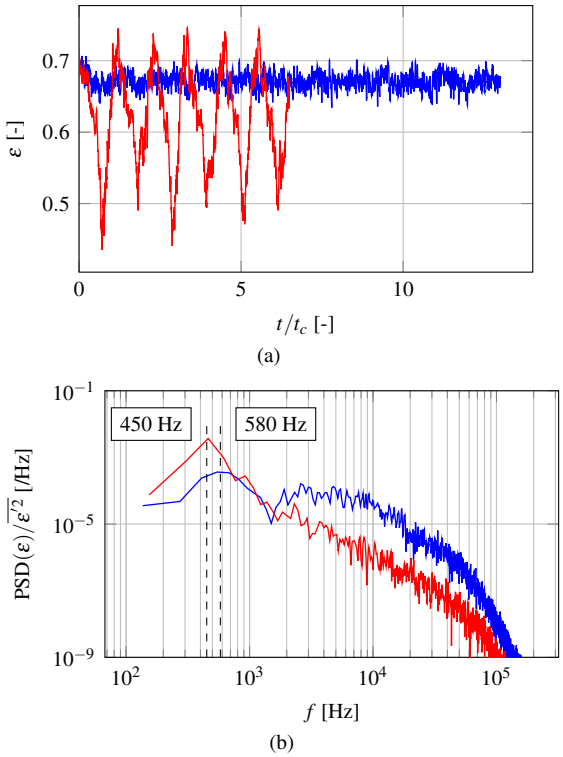

Figure 9: Time evolution (a) and PSD (b) of the mass flow rate for (——) $TR = 0.72$ (little buzz) and (——) $TR = 0.70$ (big buzz).

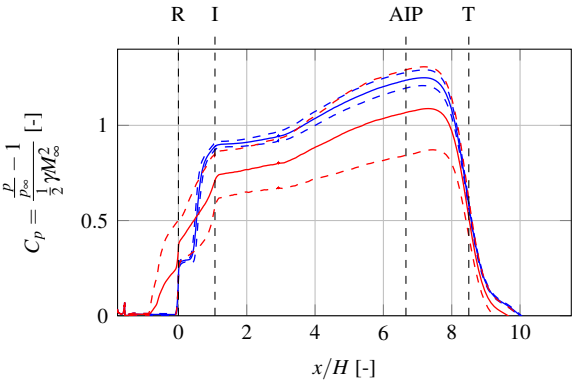

Figure 10: Pressure coefficient distribution on the lower wall (——) $TR = 0.72$. (——) $TR = 0.70$. (Solid line) Time-averaged distribution. (Dashed line) RMS envelope.

in order to highlight the shock structure. It can be seen that the shock is located at the middle of the compression ramp which allows for spillage of the exceeding incoming mass flow with respect to the critical mass flow rate of the throat. The interaction with the boundary layer generates a classical λ-structure at the shock foot. The interaction occurs for a local upstream Mach number of 1.45 which is high enough to induce flow separation, as represented by the red line in Fig. 11. As the flow enters the inlet, the flow separation is further amplified due to the flow deviation imposed by the diffuser ramp. The reattachment point is located far downstream at $x/H \approx 5.5$ owing to the adverse pressure gradient in the subsonic diffuser. The presence of a large separated area generates a longitudinal shear layer that starts at the shock foot and grows in the axial direction. It can be seen in Fig. 11b that the shear layer corresponds to high values of the turbulent kinetic energy. The terminal shock itself exhibits high value of TKE which can be attributed to its back and forth motion. We can see on the Schlieren visualization (Fig. 11c) that the terminal shock and its foot are blurred over a certain extent which is an other indication of the shock motion.

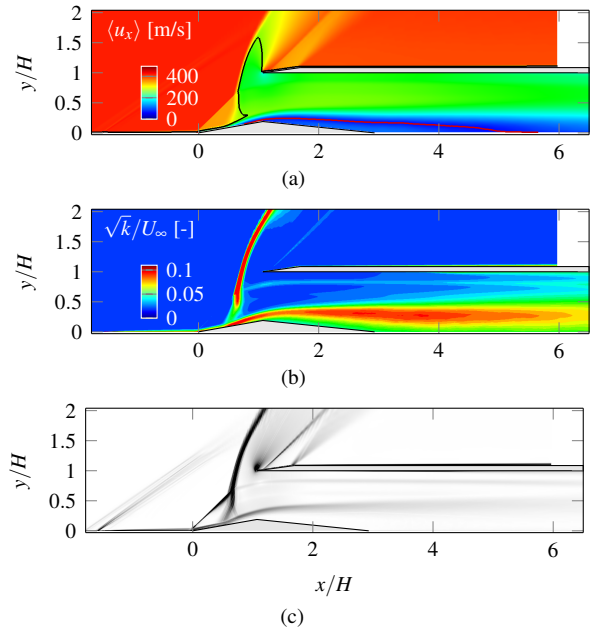

Figure 11: Mean (a) and fluctuating velocity (b) fields and (c) numerical Schlieren for TR = 0.72. (Black line) Sonic line. (Red line) Separation line ($u_x = 0$).

In order to investigate the flow mechanisms related to the shock motion, we concentrate on the time evolution of the pressure footprint on the lower wall. For each instant, the instantaneous pressure field is averaged in transverse direction Oz. Fig. 12a shows the spatio-temporal map of the transverse-averaged pressure coefficient on the lower wall. The excursion of the terminal shock foot is highlighted by the black line corresponding to $C_p = 0.4$. The frequency spectrum of the shock longitudinal position exhibits a marked peak at 600 Hz (not shown here). No other pertinent information can be inferred from this map because the pressure fluctuations are an order of magnitude lower than the mean axial pressure variation due to the flow deceleration in the

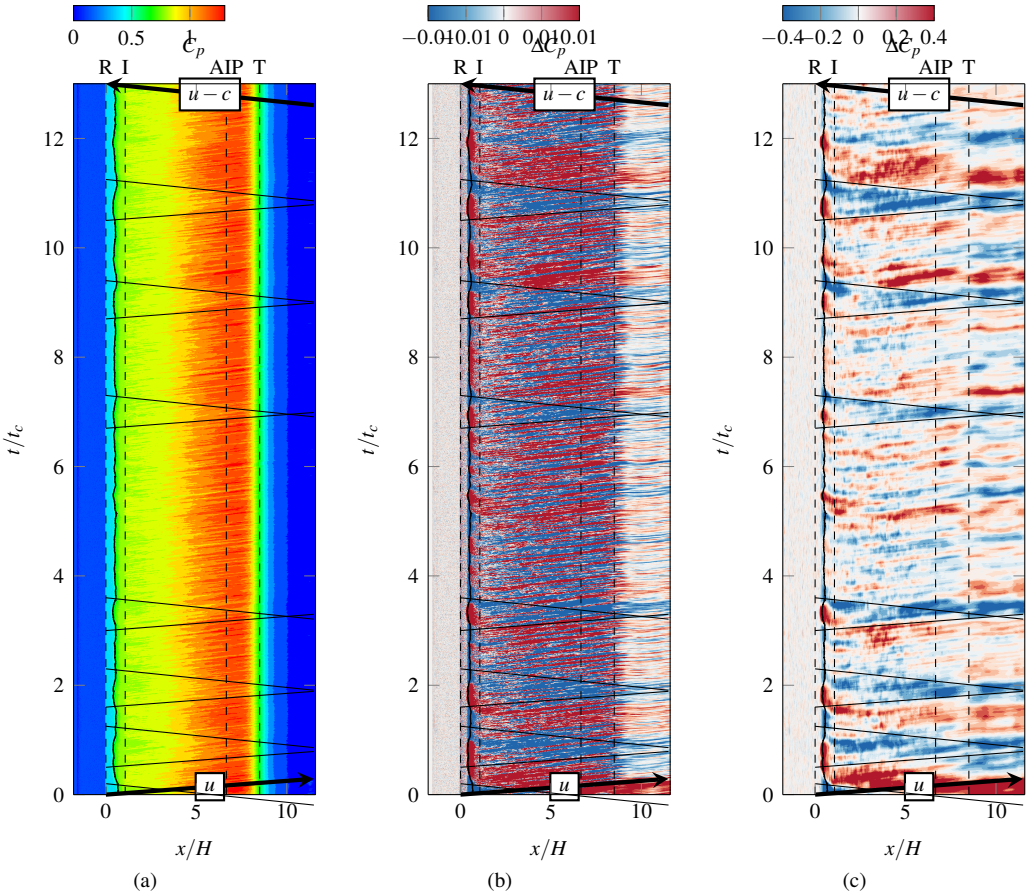

Figure 12: Spatio-temporal map of the pressure fluctuations along the inlet at TR = 0.72. (a) Pressure. (b) Fluctuating pressure. (c) Time-filtered fluctuating pressure.

diffuser. For this reason, the mean pressure has been subtracted from the unsteady pressure field for each axial position. The corresponding spatio-temporal map is plotted in Fig 12b. It can be seen that the terminal shock back-and-forth motion corresponds to successive positive and negative fluctuations depending whether it is moving forward or backward. In the duct, one can observe alternating positive and negative pressure fluctuations over large time period. We retrieve that the amplitude of the pressure fluctuations is low at the chocked throat as already noticed hereabove. The low-frequency fluctuations are nonetheless superimposed with fluctuations of the same order of magnitude but at higher frequency. The latter corresponds to the hydrodynamic pressure fluctuations generated by the shear layer. In order to isolate the low-frequency large-scale mechanisms in the flow, the pressure signals have been time-filtered by means of the second order Savitzky-Golay filter with a cut-off frequency of $2000Hz$. The filtered spatio-temporal map is presented in Fig 12c. Low-frequency pressure fluctuations in the duct are now clearly evidenced, with alternating flow expansion and compression.

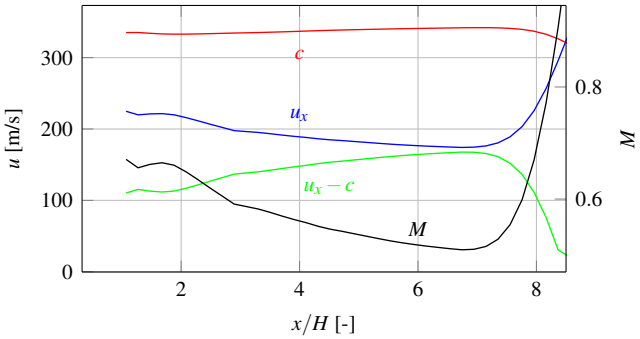

Figure 13: Mean propagation velocities and Mach number along the duct.

Spatio-temporal maps constitute a convenient way to highlight how the pressure waves propagates in the flow. In a compressible fluid flow, the information generally propagates along the characteristic velocities which are in a one-dimensional case u, $u + c$ and $u - c$, with u the convection velocity and c the speed of sound. In Fig. 13,

we have plotted the longitudinal evolution of the some characteristic velocities along the x-axis in the duct. For each axial location the velocities are averaged over the height of the duct. Although the speed of sound is relatively constant in the duct, the u_x and $|u_x - c|$ velocity changes significantly. We can nevertheless compute their average value over the whole duct, that yields: $u_x = 192$ m/s, $u_x - c = -147$ m/s. These two mean propagating velocities have been reported in the spatio-temporal map (Fig. 12). It can be seen that for several little buzz cycle the expansion wave (negative pressure fluctuation) seems to propagate from the inlet section towards the chocked throat at the mean convection speed u_x. On the contrary, the compression wave (positive pressure fluctuation) propagates upstream from the throat towards the inlet section at the mean speed $u_x - c$. This observation corroborates the findings of Candon *et al.* [1] who have highlighted the role of an upstream-propagating compression wave in the shock motion in a near-critical flow configuration.

In order to better describe the mechanisms associated with a little buzz cycle, we presents in Fig. 14a a close-up view of the filtered spatio-temporal map for four repetitions of the low-frequency unsteadiness. The filtered pressure footprint on the upper wall is also represented in Fig. 14b. The filtered footprint are very similar on both upper and lower wall, which indicates the large-scale feature of the low-frequency pressure waves. Time evolution of the mass flow rate at AIP is represented in Fig. 14c. The following scenario for the little buzz cycle can then be inferred:

1. An upstream-propagating compression wave causes the terminal shock to move upstream, which translates into a pressure increase on the compression ramp

2. As the shock moves upstream the captured mass flow ratio diminishes which in turn induces a strong pressure drop at the inlet section.

3. The expansion wave propagates from the inlet section towards the throat at the mean convection speed

4. In the same time the shock continues to move upstream, reaches its most advanced position.

5. As the captured mass flow ratio is lower than the critical mass flow at the chocked throat section, the shock starts to move back.

6. This downstream motion ends when a new upstream-propagating compression wave causes it to move upstream.

It can bee see from Fig. 14a that velocity of the upstream and downstream motion of the terminal shock are one order of magnitude lower to that of the pressure waves in the duct. This could explain why the observed frequency for the little buzz is inferior to the fundamental acoustic frequency f_0 of a duct, which consider that the information propagates at characteristic speeds. In the present case, part of the feedback mechanism involves a low speed motion of the terminal shock on the compression ramp.

3.2.2 Big buzz

We now concentrate on the big buzz regime obtained for TR $= 0.70$. The spatio-temporal map of both the pressure coefficient and the pressure fluctuations on the lower wall along with the time evolution of the mass flow ratio are represented in Fig. 15. The instantaneous fields of both Mach number and numerical Schlieren corresponding to different characteristic times are shown in Figs. 16 and 17. The simulation has been initialized (time $t = 0$) with the final solution obtained for TR $= 0.72$ (little buzz regime), which allows to investigate the transient behaviour of the air inlet as the throat is throttled from TR $= 0.72$ to 0.70.

Because of the reduction of the critical mass flow ratio, the pressure increase at the end of the subsonic diffuser induces a forward motion of the terminal shock (b). It moves up to the beginning of the compression ramp ($x = 0$) and even continues further upstream by generating a stronger flow separation on the flat plate (c). This large separated area induces the appearance of a weak oblique shock whose angle is higher than that of the oblique shock generated by the ramp, which contributes to the large amount of flow spillage above the inlet cowl and the subsequent drop in the mass flow ratio at the AIP. The terminal shock lies now in the vicinity of the inlet section. As spillage prevents the exceeding incoming flow from entering the inlet, the pressure in the subsonic diffuser decreases which leads to a backward motion of the shock. As the oblique shock moves downstream flow separation disappears on the flat plate and when it has passed the beginning of the compression ramp the shock system exhibits again a λ-pattern with separation on the compression ramp. The backward motion ends when the terminal shock has nearly reached the inlet section (d). In this state, the air inlet is close to the critical regime where the captured streamtube corresponds to the captation area. The ingested mass flow ratio is then higher than the critical mass flow ratio of the sonic throat. This excess leads to a new increase in the static pressure at the end of the subsonic diffuser which induces in turn the forward motion of the shock (e-f) that initiates a new cycle. It is noteworthy that the next buzz cycles exhibit the same features both in terms of intensity and flow structure as the first one initiated by the transient associated with the reduction of the throat critical section. This is in contrast to what have been observed in experimental buzz studies [14, 2] on isolated rectangular air inlets where buzz

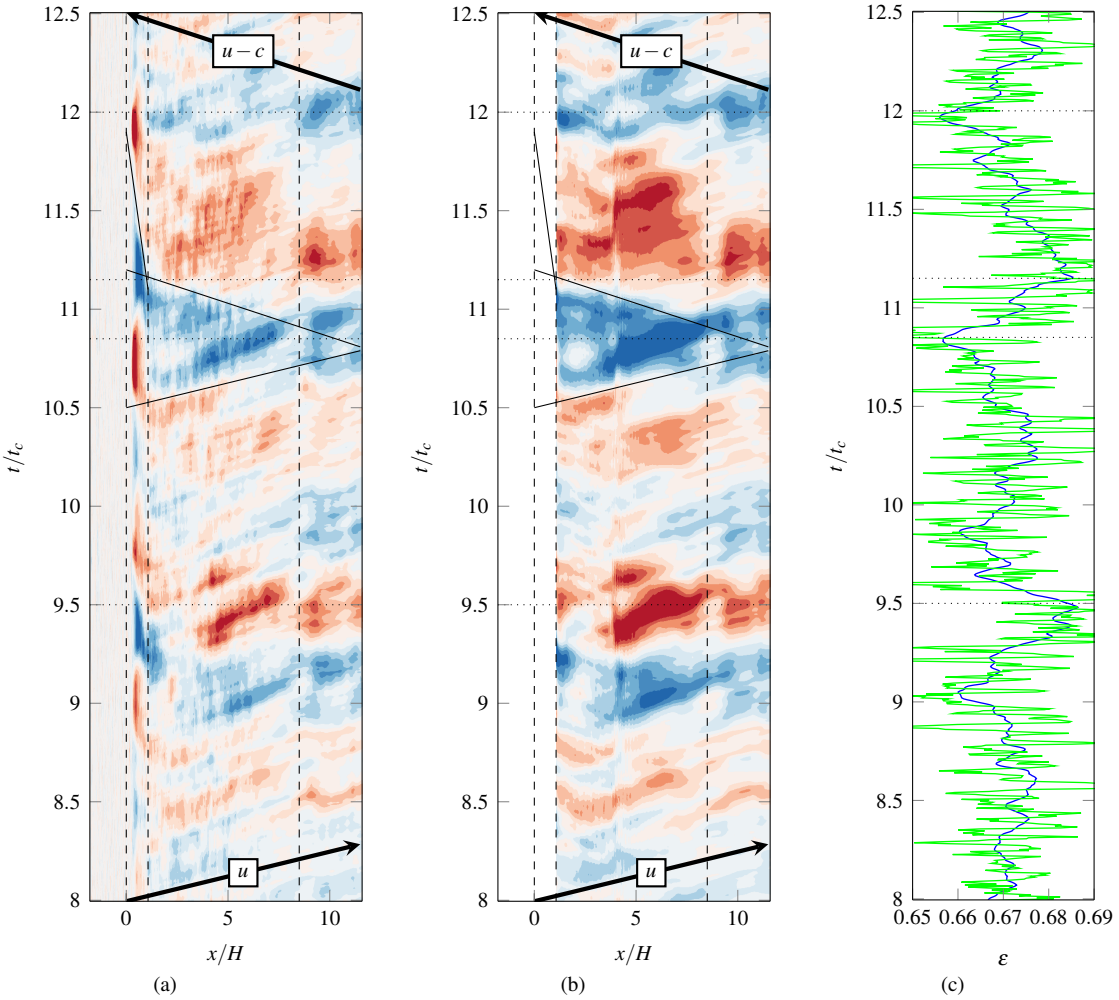

Figure 14: Filtered spatio-temporal map of the pressure fluctuation on the lower (a) and upper (b) walls at TR = 0.72. (c) Filtered (——) and unfiltered (——) time-evolution of the normalized mass flow ratio through AIP.

pressure oscillations grow progressively until a limit cycle is reached. The violent buzz triggering observed in our case is certainly due to the presence of the upstream flat plate and the associated boundary layer that rapidly generate a large amount of flow spillage due to the strong flow separation. We can then conclude that buzz mechanism in our case is of Dailey type. The effect of the shock-intersection generated shear layer, generally associated to the Ferri-type buzz onset, seems to have little effect on the flow.

As for the little buzz analysis, the spatio-temporal map in Fig. 15 allows to investigate the propagation speed of the information in the flow. It can be seen that the downstream-travelling pressure drop due to flow spillage propagates at the mean convection velocity u_x in the duct while the usptream-travelling pressure increase due to exceeding ingested mass flow ratio propagates at the mean characteristic velocity $u_x - c$. As observed for the little buzz, the terminal shock and then the oblique shock on the flat plate progress forward an order of magnitude slower than pressure waves in the subsonic diffuser. As the shock excursion is greater, the time required for the shock to travel to its most upward location is longer which in turn increases the period of a cycle and then reduces the buzz frequency compared to the little buzz frequency.

A detailed analysis of Fig. 15 shows that, in the phase associated with the downstream motion of the shock, a pressure rise arises at the beginning of the duct and propagates downstream at about speed u_x. This phenomenon can be related to the appearance of a second terminal shock (d) located in the duct. It is due to the flow acceleration from subsonic behind the terminal shock on the compression ramp to supersonic velocity, owing to the effective contraction of flow induced by the flow separation shear layer. It is also seen in Fig. 16d that the second strong shock in the duct triggers the transition of the boundary layer on the upper wall.

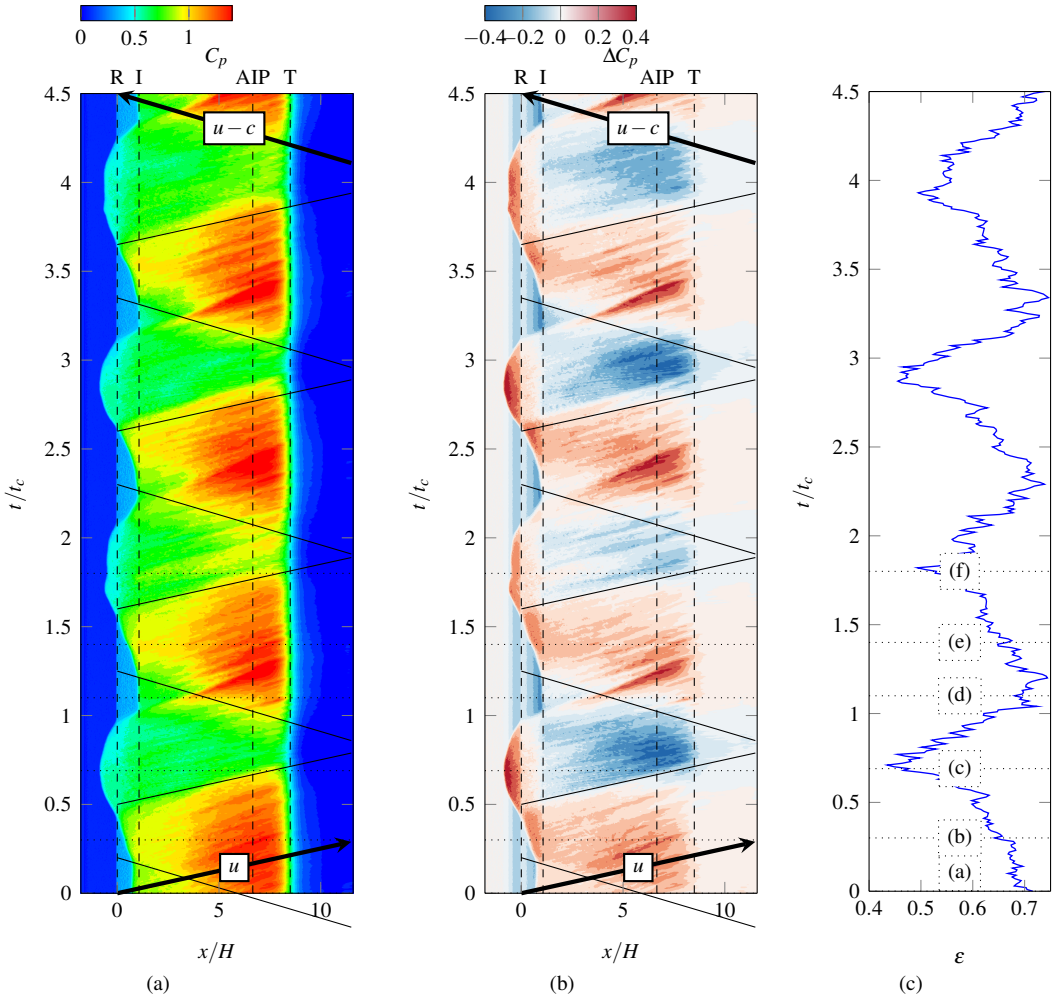

Figure 15: Spatio-temporal map of the pressure fluctuations along the inlet at TR = 0.70.

4. CONCLUSIONS

In this study, we have carried out Large-Eddy Simulations of a rectangular supersonic air inlet for two throttling ratios which allow to reproduce both big buzz and little buzz regimes. The geometry differs from classical inlets by the presence of a turbulent boundary layer that develops on a flat plate ahead of the compression ramp. We have verified that the boundary layer, numerically triggered by a rough patch, is well developed prior to any shock interaction by comparison with reference DNS data. An in-depth analysis of the pressure fluctuations has permitted to highlight the flow mechanisms that take place in both regimes and their link with the dominant frequency. In both regimes, the back and forth motion of the terminal shock is associated with a downstream expansion wave propagating in the subsonic diffuser at the mean convection velocity and an upstream-propagating compression wave. The shock motion on the external surfaces (ramp and/or flat plate) is much slower than the duct pressure waves which could explain that the observed frequencies of buzz are lower than the fundamental acoustic mode based on the duct length.

ACKNOWLEDGEMENT

This work has been funded by the Onera research project PR-OPOSSUM dedicated to the prevision and control of supersonic air inlets. The author is thankful to I. Mary for his technical support with the solver FastS. This work was performed using HPC resources from GENCI-CINES (Grant A0042A10399).

REFERENCES

[1] S. Candon, E. Loth, and M. Rybalko. Near-On-Design Unsteadiness in a Supersonic Low-Boom Inlet. *Journal of Propulsion and Power*, 32(2):360–372, 2016.

[2] H. Chen, H.-j. Tan, Y.-z. Liu, and Q.-f. Zhang. External-Compression Supersonic Inlet Free from

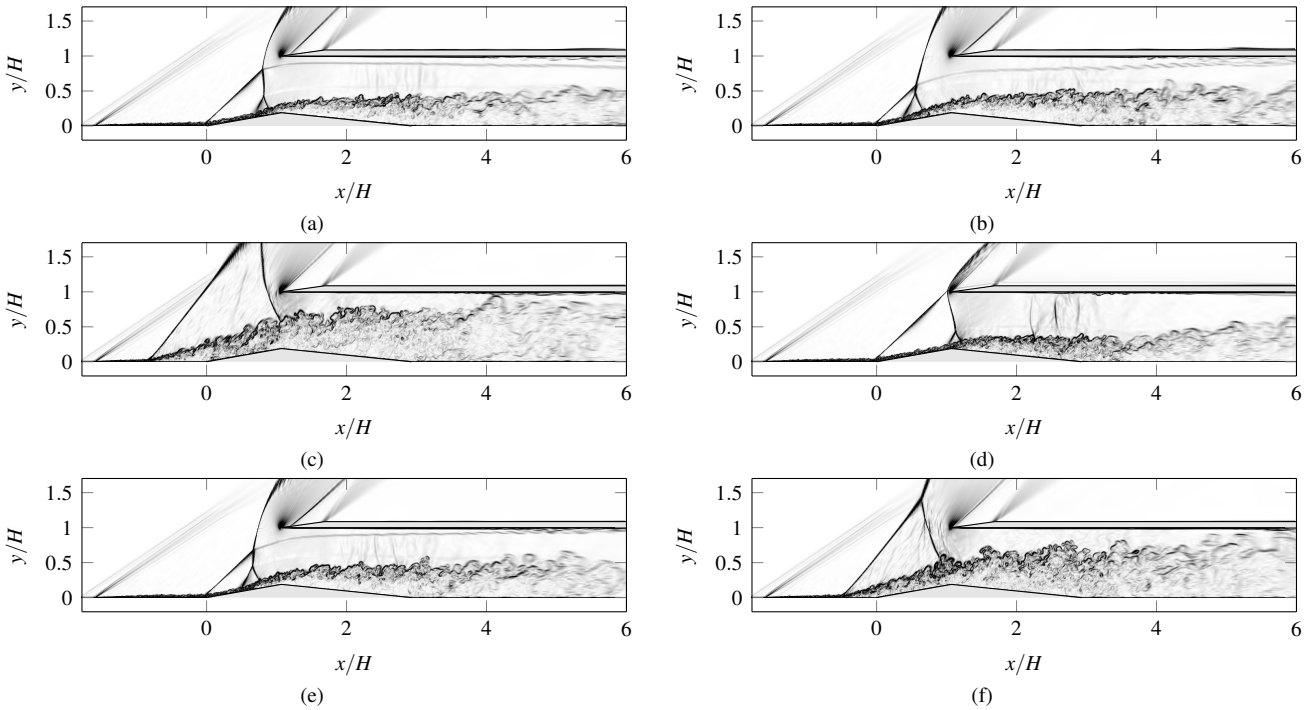

Figure 16: Numerical Schlieren at different characteristic times (see in Fig. 15c).

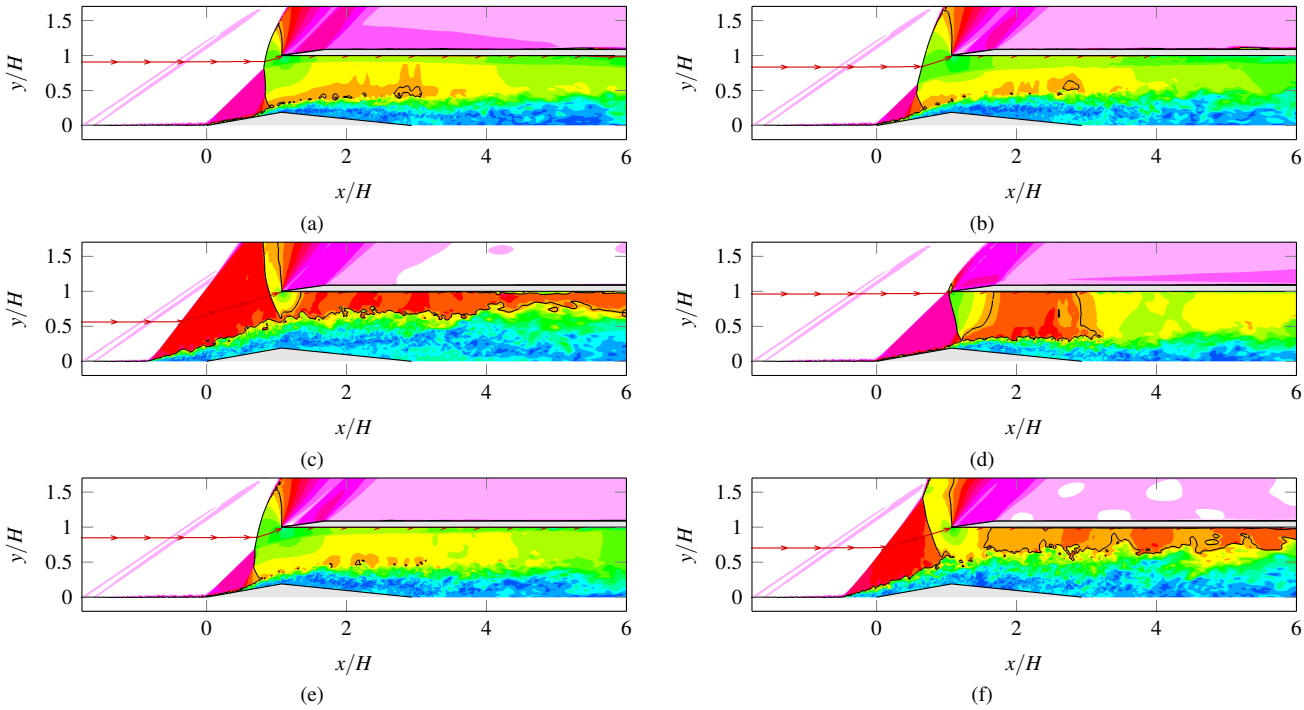

Figure 17: Instantaneous field of the Mach number at different characteristic times (see in Fig. 15c).

Violent Buzz. *AIAA Journal*, 57(6):2513–2523, June 2019.

[3] R. V. Chima. Computational Analysis of a Low-Boom Supersonic Inlet. page 21, 2011.

[4] H. Choi and P. Moin. Effects of the Computational Time Step on Numerical Solutions of Turbulent Flow. *Journal of Computational Physics*, 113(1):1–4, July 1994.

[5] C. L. Dailey. Supersonic Diffuser Instability. *Journal of the Aeronautical Sciences*, 22(11):733–749, 1955.

[6] J. Dandois, I. Mary, and V. Brion. Large-eddy simulation of laminar transonic buffet. *Journal of Fluid Mechanics*, 850:156–178, Sept. 2018.

[7] A. Ferri and L. M. Nucci. The Origin of Aerodynamic Instability of Supersonic Inlets at Subcritical Conditions. Technical Report NACA RM-L50K30, 1951.

[8] P. Grenson and S. Beneddine. Analysis of shock oscillations of an external compression supersonic inlet through unsteady numerical simulations. In *2018 Applied Aerodynamics Conference*. American Institute of Aeronautics and Astronautics, June 2018.

[9] P.-J. Lu and L.-T. Jain. Numerical Investigation of Inlet Buzz Flow. *Journal of Propulsion and Power*, 14(1):90–100, 1998.

[10] I. Mary and P. Sagaut. Large Eddy Simulation of Flow Around an Airfoil Near Stall. *AIAA Journal*, 40(6):1139–1145, 2002.

[11] R. W. Newsome. Numerical Simulation of Near-Critical and Unsteady, Subcritical Inlet Flow. *AIAA Journal*, 22(10):1375–1379, 1984.

[12] P. Schlatter and R. Örlü. Assessment of direct numerical simulation data of turbulent boundary layers. *Journal of Fluid Mechanics*, 659:116–126, Sept. 2010. Publisher: Cambridge University Press.

[13] S. Trapier, S. Deck, and P. Duveau. Delayed Detached-Eddy Simulation and Analysis of Supersonic Inlet Buzz. *AIAA Journal*, 46(1):118–131, 2008.

[14] S. Trapier, P. Duveau, and S. Deck. Experimental Study of Supersonic Inlet Buzz. *AIAA Journal*, 44(10):2354–2365, 2006.